Journal of Power Sources 185 (2008) 1179–1192

Contents lists available at ScienceDirect

Journal of Power Sources

journal homepage: www.elsevier.com/locate/jpowsour

A segmented model for studying water transport in a PEMFC

Yong-Song Chen, Huei Peng*

Department of Mechanical Engineering, University of Michigan, 1231 Beal Avenue, Ann Arbor, MI 48109-2121, USA

ARTICLE INFO

Article history:
Received 31 May 2008
Received in revised form 2 July 2008
Accepted 3 July 2008
Available online 19 July 2008

Keywords:
PEM fuel cell
Water management
Humidity
Model
Neutron radiography

ABSTRACT

Water management plays an important role in the durability and efficiency of a proton exchange membrane fuel cell (PEMFC). In this study, a single cell is modeled as a lumped model consisting of 15 interconnected segments, which are linked according to the flow field patterns of the anode and cathode but they are treated as lumped elements individually. Parameters of this model were calibrated based on neutron radiography experimental results obtained at the NIST Center for Neutron Research (NCNR). The model can be used to predict distributions of current density, water content in the membrane, relative humidity (RH) in the flow channels, and water accumulation in the gas diffusion layer (GDL).

1. Introduction

Many factors influence the performance of proton exchange membrane fuel cells (PEMFCs), including membrane material and thickness, platinum loading, flow field designs, temperature, reactant partial pressure, etc. In addition, a critical issue that has severely limited the application of PEMFCs is its poor reliability under cyclic temperature and humidity operations. An important factor that influences both the nominal performance and life under transient loading is the water accumulation and distribution in a PEMFC. When the fuel cell has too little or too much water, both performance and reliability suffers. Water accumulation also influences the warm-up and shutdown procedure for PEMFCs that need to work in below-freezing temperature. It is fair to say that in addition to the cost issue, water management is one of the most important remaining issues for the adoption of PEMFCs. Many models have been developed over the past several years for the water/humidity behavior inside a PEMFC.

Bernardi and Verbrugge [1,2] developed one of the early steady-state, one-dimensional mathematical models. Their model describes reactant transport in the GDLs and water transport in a PEMFC. The membrane was assumed to be fully hydrated, which is different from practical working conditions of PEMFCs, especially for the anode side. Springer et al. [3] empirically related membrane conductivity to water content of the Nafion membrane. Many of the subsequently developed models used this empirical relationship to determine the conductivity of the Nafion membrane, even for membranes with different thickness. Fuller and Newman [4] developed a two-dimensional model to discuss water management, thermal management and fuel utilization in a PEMFC. Gurau et al. [5] developed a two-dimensional model, which discussed reactant concentrations in the through-MEA direction and along the flow channel direction. Um et al. [6] and Wang et al. [7] developed models based on computational fluid dynamics (CFD) and solved the equations numerically. Um et al. [8] also extended their work to a three-dimensional model to study the performance of an interdigitated flow field design. Their results show that forced convection of gases through GDL helps to improve performance at high current densities. None of the models discussed above considered the effect of water accumulation on cell performance.

Starting from around the turn of the century, models that include the water/humidity behavior start to appear in the literature. Baschuk et al. [9] developed a model with the effect of variable degree of water flooding in the cathode catalyst layer and cathode GDL on cell performance. Wang et al. [10] of the Pennsylvania State University developed a model which handles the situation where two-phase flow exists in the cathode. Pasaogullari and Wang [11] applied the two-phase flow model in the cathode GDL and investigated the effect of liquid saturation on cell performance. Wang et al. [10] and Pasaogullari and Wang [11] related capillary pressure with the Leverett's function. The two-phase flow model successfully described water vapor distribution and liquid water accumulation in the GDL and in the flow channel. However, most of these models focus on water accumulation in the GDL under the channel and the

* Corresponding author. Tel.: +1 734 936 0352; fax: +1 734 764 4256.
E-mail address: hpeng@umich.edu (H. Peng).

0378-7753/$ – see front matter © 2008 Elsevier B.V. All rights reserved.
doi:10.1016/j.jpowsour.2008.07.018

Nomenclature

a	water vapor activity
A	area (m^2)
c	concentration ($mol\,m^{-3}$)
d	hydraulic diameter (m)
D_{i-j}	diffusivity of gas pair i–j in a mixture ($m^2\,s^{-1}$)
F	Faraday's constant (96485 °C equiv.$^{-1}$)
H	channel depth (m)
i	current density ($A\,m^{-2}$)
I	current (A)
$K_{osmotic}$	electro-osmotic drag coefficient
K_{diff}	back diffusion coefficient ($mol\,s\,m^{-2}$)
K_{conv}	coefficient of convective mass transfer ($mol\,s\,m^{-2}$)
L	channel length (m)
M	equivalent weight of a dry membrane ($kg\,mol^{-1}$)
N	molar flow rate ($mol\,s^{-1}$)
P	pressure (Pa)
Q	gas volume flow rate ($m^3\,s^{-1}$)
R	universal gas constant ($8.314\,J\,mol^{-1}\,K^{-1}$)
R_j	resistance of component j (Ω)
Sh	Sherwood number
t	thickness (m)
T	temperature (K)
V	voltage (V)
W	channel or rib width (m)
x_j	molar fraction of species j
y_{O_2}	percentage of oxygen in the air
Z	channel number in a segment

Greek letters

α_c	transfer coefficient
ε	porosity of gas diffusion layer
φ	relative humidity
λ	water content
μ	dynamic viscosity ($kg\,m^{-1}\,s^{-1}$)
ρ	density ($kg\,m^{-3}$)
σ	electrical conductivity ($\Omega^{-1}\,m^{-1}$)
ζ	stoichiometry of gas

Subscripts

an	anode
act	activation
avg	average
c	critical
ca	cathode
cap	capillary
c/g	channel and gas diffusion layer interface
ch	channel
contact	contact
conc	concentration
gdl	gas diffusion layer
g/m	gas diffusion layer and membrane interface
H_2	hydrogen
H_2O	water
in	inlet
limit	limit
N_2	nitrogen
ohm	ohmic
out	outlet
O_2	oxygen
p	pore
pem	proton exchange membrane
plate	plate
sat	saturation
seg	segment
v	water vapor
w	liquid water

developed formula do not apply readily to the subspace under the rib.

Natarajan and Nguyen [12] from the University of Kansas proposed a model that included the effect of water accumulation in the GDL under the rib and under the channel on cell performance. In their model, instead of using the Leverett's function, they suggested another empirical equation to describe the capillary pressure. Later, the same group [13,14] further simplified capillary pressure gradient in their models as a constant. Their results showed significant difference with studies using the Leverett's function. Thus, experimental data that clearly describe water accumulation in the GDL, for both along the flow direction and across the GDL direction is needed. Recently, several studies used neutron radiography to detect liquid water distribution in PEMFCs [15–17]. Neutron image results showed that significant amount of liquid water could accumulate in the GDL under the ribs. Therefore, it is important to develop a model that predicts water distribution in GDL under the rib as well as under the flow channel.

Because the reactant concentration varies along the flow channels, it causes variations in current density, water content, and temperature [18–20]. Therefore, the water generation and distribution in a PEMFC are not uniform. In addition, different anode and cathode flow field patterns were designed for different applications or working conditions [21–23]. Many CFD models have difficulties simulating PEMFCs with complex flow fields due to requirement of heavy numerical computation load. Currently published CFD models simulate the reaction either in a straight flow channel or in a simple flow field. Lumped models [24–26] commonly assume a uniform reaction within fuel cells and do not consider the spatial distribution of reactants. Therefore, pure CFD models or pure lumped models may not be the best modeling choice.

In this study, a steady-state, segmented mathematical model was developed to describe distributions of liquid water accumulation, current density, and relative humidity (RH) in the flow channel of a PEMFC. This model was calibrated by using neutron radiography experiments to quantify liquid water in a PEMFC with the same flow field pattern. Water transport in the MEA and the influence of RH of cathode inlet is also discussed in this study.

2. Mathematical model

To capture distributed characteristics of a PEMFC, the active area is divided into 15 segments that are connected according to flow fields, as shown in Fig. 1. Each segment is viewed as a small lumped model, i.e. reactant/membrane properties and reaction in each segment are assumed to be uniform. The segments are connected together based on the flow direction of the reactants. Since each is regarded as a lumped model, it cannot account for the rib effects on gas transport. However, we will introduce semi-empirical correlation to describe the rib effects on water accumulation.

The inputs of a segment are the outputs of the preceding segments. For the overall cell, input variables are stoichiometry value, RH, and temperatures of the inflow gas and cell temperature. According to the experiment of Wang et al. [27], temperature difference between upper stream and down stream is less than 2 °C when

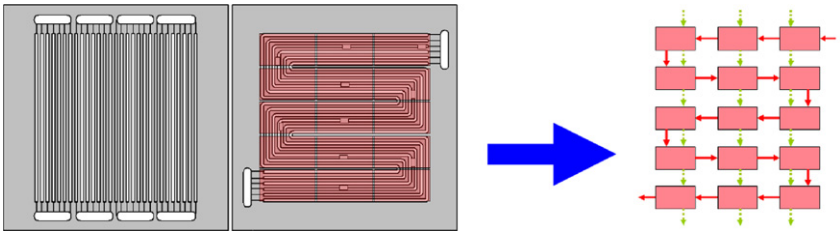

Fig. 1. Schematic of a single cell modeled as several small segments.

cell current density is 0.74 A cm^{-2}. The study of Chen and Peng [28] also shows uniformly distributed temperature in a single cell; thus, all segment temperatures are assumed the same and constant as operating temperature. The assumptions are summarized below:

1. The model describes steady-state conditions.
2. The ideal gas law was employed for gas mixture.
3. Temperature throughout the single cell is uniformly distributed.
4. Chemical reaction throughout the segment is uniform.
5. Rib effects on gas transport and gas transport in the flow channel direction are neglected. Only gas transport through the MEA direction is considered in each segment.

Based on the desired cell current and operating conditions, the molar flow rates of inflow hydrogen and oxygen for a single cell are evaluated as

$$N_{\mathrm{an,H_2,in}} = \frac{I_{\mathrm{cell}}}{2F}\zeta_{\mathrm{an}} \tag{1}$$

$$N_{\mathrm{ca,O_2,in}} = \frac{I_{\mathrm{cell}}}{4F}\zeta_{\mathrm{ca}} \tag{2}$$

where N is the molar flow rate in mol s^{-1}, ζ_{an} and ζ_{ca} are stoichiometry of anode and cathode, respectively, and F is the Faraday constant.

If air is used as the cathode reactant, the nitrogen molar flow rate is calculated from

$$N_{\mathrm{ca,N_2,in}} = N_{\mathrm{ca,O_2,in}}\frac{1-y_{\mathrm{O_2}}}{y_{\mathrm{O_2}}} \tag{3}$$

where $y_{\mathrm{O_2}}$ is the percentage of oxygen in the air. For an operating condition at selected inlet relative humidity φ and pressure P, the molar fraction of inlet vapor can be calculated from

$$x_{\mathrm{an,v,in}} = \frac{\varphi_{\mathrm{an,in}}P_{\mathrm{v,sat}}}{P_{\mathrm{an,in}}} \tag{4}$$

$$x_{\mathrm{ca,v,in}} = \frac{\varphi_{\mathrm{ca,in}}P_{\mathrm{v,sat}}}{P_{\mathrm{ca,in}}} \tag{5}$$

where $P_{\mathrm{v,sat}}$ is the saturated vapor pressure, which is a function of working temperature. The value of $P_{\mathrm{v,sat}}$ is calculated from the following equation, given in Ref. [3]:

$$P_{\mathrm{v,sat}} = 1.013\times10^{5} \times 10^{[-2.1794+0.02953T_{\mathrm{seg}}-9.1837\times10^{-5}T_{\mathrm{seg}}^2+1.4454\times10^{-7}T_{\mathrm{seg}}^3]} \tag{6}$$

The inlet water molar flow rate can then be calculated from

$$N_{\mathrm{an,w,in}} = \frac{x_{\mathrm{an,v,in}}}{1-x_{\mathrm{an,v,in}}}N_{\mathrm{an,H_2,in}} \tag{7}$$

$$N_{\mathrm{ca,w,in}} = \frac{x_{\mathrm{ca,v,in}}}{1-x_{\mathrm{ca,v,in}}}(N_{\mathrm{ca,O_2,in}}+N_{\mathrm{ca,N_2,in}}) \tag{8}$$

Eqs. (1)–(8) describe required amount of inflow species. After fed into the first segment of a fuel cell, gases flow through each segment based on the flow fields of anode and cathode to the subsequent segment.

Species flow in each segment is shown in Fig. 2. Each segment itself consists of six interacting sub-models: cathode flow channel, anode flow channel, cathode GDL, anode GDL, membrane hydration, and segment voltage. Theses models will be described in the following sections.

2.1. Anode/cathode channel model

The channel model describes the reactant behavior inside the anode and cathode of a segment. The model uses the molar conservation principle and fluid dynamic properties to calculate the outflow properties and pressure drop along the flow channels. The pressure drop of the gas mixture in the flow channels was frequently ignored in earlier models; however, in practice it is one of the key parameters in designing a fuel cell and is related to the selection of the air pump and the calculation of efficiency of a fuel cell system.

The segment current, I_{seg}, is an input based on which the segment model can be simulated. The amount of consumed reactants in the segment can be determined by

$$N_{\mathrm{an,H_2,react}} = \frac{I_{\mathrm{seg}}}{2F} \tag{9}$$

$$N_{\mathrm{ca,O_2,react}} = \frac{I_{\mathrm{seg}}}{4F} \tag{10}$$

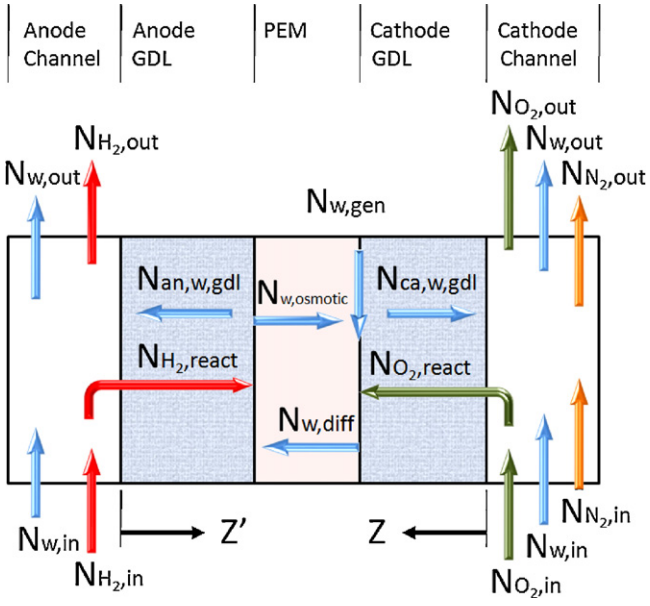

Fig. 2. Species transport in a segment of this model.

The amount of water generation at the cathode catalyst layer can be expressed as

$$N_{ca,w,gen} = \frac{I_{seg}}{2F} \tag{11}$$

Then the molar outflow rate can be calculated from

$$N_{an,H_2,out} = N_{an,H_2,in} - N_{an,H_2,react} \tag{12}$$

$$N_{ca,O_2,out} = N_{ca,O_2,in} - N_{ca,O_2,react} \tag{13}$$

$$N_{an,w,out} = N_{an,w,in} - N_{an,w,gdl} \tag{14}$$

$$N_{ca,w,out} = N_{ca,w,in} - N_{ca,w,gdl} \tag{15}$$

The water molar flow rates $N_{an,w,gdl}$ and $N_{ca,w,gdl}$ through GDL in Eqs. (14) and (15) are calculated by the gas diffusion layer (GDL) model.

The pressure drop due to friction for a continuous, straight channel with length L can be calculated from the following equation [29]:

$$\Delta P = 32 \int_0^L \frac{\mu(y)Q(y)}{ZA_{ch}d_{ch}^2} dy \tag{16}$$

where the reactant is consumed along the flow channel direction y. As a first-order approximation, we assume that dynamic viscosity $\mu(y)$ and flow rate $Q(y)$ of gas mixtures vary linearly along the flow channel:

$$\mu(y) = \mu_{in} - \frac{y}{L}(\mu_{in} - \mu_{out}) \tag{17}$$

$$Q(y) = Q_{in} - \frac{y}{L}(Q_{in} - Q_{out}) \tag{18}$$

where μ_{in} and μ_{out} are the dynamic viscosities of the mixture at the inlet and outlet, respectively, and can be calculated by the mixture properties

$$\mu = \sum_i x_i \mu_i \tag{19}$$

where x_i is the molar fraction of species i. Similarly, the mixture flow rates at inlet Q_{in} and outlet Q_{out} can be expressed in terms of the ideal gas law:

$$Q = \frac{RT}{P} \sum_i N_i \tag{20}$$

After substituting Eq. (17) and Eq. (18) into Eq. (16), and integrating the equation, the pressure drop along the channel was found to be

$$P_{in} - P_{out} = \frac{16L}{3ZA_{ch}d_{ch}^2}[Q_{in}(2\mu_{in} + \mu_{out}) + Q_{out}(\mu_{in} + 2\mu_{out})] \tag{21}$$

The outflow pressure can be determined by Eq. (21), and the average pressure in a segment can be calculated by

$$P_{avg} = \frac{1}{2}(P_{in} + P_{out}) \tag{22}$$

From discussion above, molar flow rates of every species and pressure at the segment outlet are determined. These properties are used as inflow properties for the subsequent segment.

2.2. Anode/cathode gas diffusion layer model

Because GDLs are made of porous media, we need to consider the effect of porous media on diffusion of gas mixtures. Each species has different diffusivity, so the molar fraction of species will vary along the diffusion path. The purpose of the GDL model is to calculate the molar fraction at the GDL/membrane interface. Furthermore, by knowing average pressure, we can determine the partial pressures of hydrogen (using the anode GDL model) and oxygen (cathode GDL model) as well as water activity for either. The hydrogen and oxygen partial pressures are used in the segment voltage model. Water activity is used in the membrane hydration model to determine water transport through the membrane.

Water transport from the membrane to the channel via GDL in two forms: gas and liquid; therefore, we need to consider under-saturated and saturated conditions separately. At under-saturated conditions, water vapor transport direction depends on the RH in the channel and at the membrane/GDL interface. At saturated condition, water generated in the catalyst layer will transport through the GDL in liquid form. The liquid water in the GDL not only induces higher resistance to gas diffusion but also covers part of the activation sites on the catalyst layer and results in reduced cell voltage.

The Stefan–Maxwell equation is used to describe diffusion of multi-component gas mixtures through the GDL [30]. For n-component gas diffusion through a porous medium, the molar fraction gradient of species i, is in the form:

$$\nabla x_i = RT \sum_j^n \frac{x_i N_j - x_j N_i}{PD_{i-j}^{eff}} \tag{23}$$

where N_i and N_j are molar flux of species i and j. PD_{i-j}^{eff} is the effective pressure diffusivity product of the mixture i–j in the porous medium, and it is related to that in a nonporous system PD_{i-j} by [31]

$$PD_{i-j}^{eff} = PD_{i-j}\varepsilon^{1.5} \tag{24}$$

where ε is the porosity of the GDL. The pressure diffusivity PD_{i-j} is dependent only on temperature T, and can be estimated from critical temperature T_c, critical pressure P_c and molecular weight M of components i and j with the following equation [30]:

$$PD_{i-j} = a\left(\frac{T}{\sqrt{T_{ci}T_{cj}}}\right)^b (P_{ci}P_{cj})^{1/3}(T_{ci}T_{cj})^{5/12}\left(\frac{1}{M_i} + \frac{1}{M_j}\right)^{1/2} \tag{25}$$

N_i and N_j in Eq. (23) can be the molar flux of hydrogen, oxygen, or water vapor through the GDL, and are calculated from the segment current and the membrane hydration model.

2.2.1. Under-saturated condition

In the anode GDL, which contains hydrogen and water vapor, the water vapor molar fraction gradient is expressed by the Stefan–Maxwell equation:

$$\frac{dx_{v,gdl}}{dz'} = \frac{RT_{seg}}{P_{an,avg}D_{H_2-v}}(x_{v,gdl}N_{H_2,gdl} - x_{H_2,gdl}N_{v,gdl}) \tag{26}$$

The direction z' is defined in Fig. 2.

Since the sum of the molar fractions of all species is equal to 1, for anode we have

$$x_{v,gdl} + x_{H_2,gdl} = 1 \tag{27}$$

In Eq. (26), $N_{v,gdl}$ is the molar water transport determined by the membrane hydration model, and hydrogen molar flux through the GDL is equal to the reacted hydrogen rate and is calculated by Eq. (9). Eq. (26) can be simplified by defining

$$B_1 \equiv -\frac{RT_{seg}}{P_{an,avg}D_{v-H_2}}(N_{H_2,gdl} + N_{v,gdl}), \tag{28}$$

$$B_2 \equiv \frac{RT_{seg}}{P_{an,avg}D_{v-H_2}}N_{v,gdl} \tag{29}$$

Given the boundary condition $x = x_{v,c/g}$ at $z' = 0$, the water vapor molar fraction profile in the GDL is

$$x_{v,gdl}(z') = \frac{B_2}{B_1} + \exp(-B_1 z')\left(x_{v,c/g} - \frac{B_2}{B_1}\right) \tag{30}$$

The above equation describes the distribution of water vapor molar fraction across the anode GDL due to water vapor flux and hydrogen flux. At the GDL/membrane interface, $z' = t_{gdl}$, the value of the water vapor molar fraction is

$$x_{v,g/m} = \frac{B_2}{B_1} + \exp(-B_1 t_{gdl})\left(x_{v,c/g} - \frac{B_2}{B_1}\right) \tag{31}$$

Given the water vapor molar fraction at the GDL/membrane interface, we can calculate water activity at the same location:

$$a_{an,v,g/m} = \frac{x_{v,g/m} P_{an,avg}}{P_{v,sat}} \tag{32}$$

The hydrogen partial pressure at the GDL/membrane interface is an important parameter to calculate segment voltage and it is determined from

$$P_{an,H_2,g/m} = P_{an,avg}(1 - x_{v,g/m}) \tag{33}$$

If the RH of gas flow in the channel is different from that at the GDL/channel interface, there will be water vapor flux in between. The molar flux of water vapor at the GDL/channel interface depends on the inflow RH and is obtained from

$$N_{v,conv} = K_{conv}(x_{c/g} - x_{in})A_{seg,conv} \tag{34}$$

where the convective mass transfer coefficient K_{conv} is defined by the Sherwood number.

$$K_{conv} = Sh\ c\, D_{ij}\, d_{ch} \tag{35}$$

where D_{ij} is the diffusivity of species i in the flow gas j. For laminar flow and constant surface temperature conditions in a fuel cell, the Sherwood number Sh is constant and is equal to 3.21 [32].

In the cathode, three species are flowing in the channel and their molar fraction gradients across the GDL are calculated from the Stefan–Maxwell equation:

$$\frac{dx_{O_2,gdl}}{dz} = \frac{RT_{seg}}{P_{ca,avg}}\left(\frac{x_{O_2,gdl}N_{v,gdl} - x_{v,gdl}N_{O_2,gdl}}{D_{O_2-v}} + \frac{x_{O_2,gdl}N_{N_2,gdl} - x_{N_2,gdl}N_{O_2,gdl}}{D_{O_2-N_2}}\right) \tag{36}$$

$$\frac{dx_{v,gdl}}{dz} = \frac{RT_{seg}}{P_{ca,avg}}\left(\frac{x_{v,gdl}N_{O_2,gdl} - x_{O_2,gdl}N_{v,gdl}}{D_{O_2-v}} + \frac{x_{v,gdl}N_{N_2,gdl} - x_{N_2,gdl}N_{v,gdl}}{D_{v-N_2}}\right) \tag{37}$$

$$\frac{dx_{N_2,gdl}}{dz} = \frac{RT_{seg}}{P_{ca,avg}}\left(\frac{x_{N_2,gdl}N_{v,gdl} - x_{v,gdl}N_{N_2,gdl}}{D_{v-N_2}} + \frac{x_{N_2,gdl}N_{O_2,gdl} - x_{O_2,gdl}N_{N_2,gdl}}{D_{O_2-N_2}}\right) \tag{38}$$

where the direction z is defined in Fig. 2. Since nitrogen does not react, $N_{N_2,gdl} = 0$. Define

$$B_3 \equiv \frac{RT_{seg}}{P_{ca,avg}}\frac{N_{v,gdl}}{D_{O_2-v}},\quad B_4 \equiv \frac{RT_{seg}}{P_{ca,avg}}\frac{N_{O_2,gdl}}{D_{O_2-v}},\quad B_5 \equiv \frac{RT_{seg}}{P_{ca,avg}}\frac{N_{O_2,gdl}}{D_{O_2-N_2}},$$
$$B_6 \equiv \frac{RT_{seg}}{P_{ca,avg}}\frac{N_{v,gdl}}{D_{v-N_2}} \tag{39}$$

Eqs. (36) to (38) can then be expressed in the matrix form

$$\frac{d}{dz}\begin{bmatrix} x_{O_2,gdl} \\ x_{v,gdl} \\ x_{N_2,gdl} \end{bmatrix} = \begin{bmatrix} B_3 & -B_4 & -B_5 \\ -B_3 & B_4 & -B_6 \\ 0 & 0 & (B_5 + B_6) \end{bmatrix}\begin{bmatrix} x_{O_2,gdl} \\ x_{v,gdl} \\ x_{N_2,gdl} \end{bmatrix} \tag{40}$$

or

$$\frac{d\mathbf{x}}{dz} = \mathbf{B}\cdot\mathbf{x} \tag{41}$$

Eq. (41) can be solved by finding the state transition matrix

$$\mathbf{\Phi}(z) = \exp(\mathbf{B}\cdot z) \tag{42}$$

and the boundary condition at $z = 0$:

$$\mathbf{x}(0) = \begin{bmatrix} x_{O_2,c/g} \\ x_{v,c/g} \\ x_{N_2,c/g} \end{bmatrix} \tag{43}$$

The molar fraction at the GDL/membrane interface is then

$$\mathbf{x}(t_{gdl}) = \mathbf{\Phi}(t_{gdl})\cdot\mathbf{x}(0) \tag{44}$$

Once the molar fractions of reactants at the GDL/membrane interface are determined, the partial pressures of reactants can be calculated and used in the segment voltage model to determine the segment voltage.

2.2.2. Saturated condition

When the anode is saturated, we assume the vapor pressures in the channel and in the GDL are both equal to the saturated water vapor pressure. The vapor pressure is proportional to the molar fraction, so the water vapor molar fraction in the anode GDL is equal to the saturated vapor molar fraction and is constant:

$$x_{v,gdl}(z') = x_{v,sat} = \frac{P_{v,sat}}{P_{an,avg}} \tag{45}$$

Since the vapor gradient is zero, the hydrogen molar fraction is also constant and is

$$x_{H_2,gdl}(z') = 1 - x_{v,sat} \tag{46}$$

Hence the hydrogen partial pressure is

$$P_{H_2,g/m} = x_{H_2,gdl}(z')\ P_{an,avg} \tag{47}$$

Similarly, when the cathode is saturated, water vapor molar fraction is equal to the saturated molar fraction and is constant, therefore:

$$\frac{dx_{v,gdl}}{dz} = 0 \tag{48}$$

In addition the sum of molar fractions of all species is equal to one

$$x_{O_2,gdl} + x_{v,gdl} + x_{N_2,gdl} = 1 \tag{49}$$

Given that $x_{v,gdl}$ is constant, if we know the nitrogen molar fraction, the oxygen molar fraction can be determined. Then we use Eq. (38) to calculate the nitrogen molar fraction from the linear equation:

$$\frac{dx_{N_2,gdl}}{dz} = B_5 x_{N_2,gdl} \tag{50}$$

Given the boundary condition, $x_{N_2,gdl} = x_{N_2,c/g}$ at $z = 0$, the nitrogen molar fraction in the cathode GDL can be expressed as

$$x_{N_2,gdl}(z) = x_{N_2,c/g}\ \exp(B_5 z) \tag{51}$$

At $z = t_{gdl}$, the molar fraction of nitrogen at the GDL/membrane interface is calculated as

$$x_{N_2,g/m} = x_{N_2,c/g}\exp(B_5 t_{gdl}) \tag{52}$$

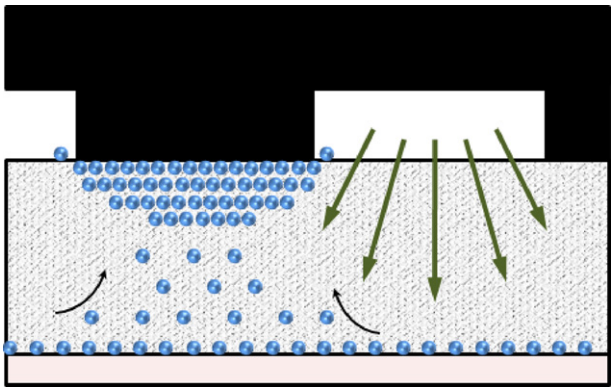

Fig. 3. Schematic of liquid water accumulation in the GDL.

The partial pressure of oxygen at the same interface is then

$$P_{ca,O_2,g/m} = P_{ca,avg}(1 - x_{v,sat} - x_{N_2,g/m}) \quad (53)$$

The presence of liquid water in the GDL will influence the diffusivity of gas. The effective diffusivity D_i^{eff} is dependent on the porosity ε and saturation s by

$$D_i^{eff} = D_i f(\varepsilon) g(s) \quad (54)$$

The saturation s is the ratio of liquid water volume to pore volume

$$s = \frac{V_w}{V_p} \quad (55)$$

Earlier studies [5,10,15,33–35] suggest the influence of porosity on diffusivity to be approximated by a polynomial relationship:

$$f(\varepsilon) = \varepsilon^{1.5} \quad (56)$$

The presence of liquid water reduces the diffusion area in the GDL and its effect is commonly modeled by a polynomial function

$$g(s) = (1 - s)^m \quad (57)$$

In this study $m = 2$ is used according to Nam and Kavinay [36].

It is clear that liquid water accumulation is an important factor that influences diffusivities of gas and cell performance. From neutron radiography experiments [15–17], water could accumulate in the GDL under the rib. Thus, we propose a hypothesis that due to the gas flow in the channels, liquid water tends to move to the GDL under the rib and accumulates close to the graphite plate/GDL interface. When the GDL cannot hold any more water, additional water generated at the membrane will push part of the water under the rib into the channel, as depicted in Fig. 3 [28]. In Ref. [28], a method to differentiate liquid water between anode and cathode in the GDL is developed based on neutron experimental data. From the test results, we observed a maximum water thickness $t_{w,max}$ accumulated in the cathode GDL under the rib. In addition, large gas flow rate in the channel is also a factor that influences water accumulation in the GDL under the rib. Thus, the average water thickness ($t_{ca,gdl,rib}$) in the GDL under the rib in a segment is approximated by

$$t_{ca,gdl,rib} = t_{w,max}\left(1 - \exp\left(\frac{\alpha N_{ca,w,gdl,rib}}{(N_{ca,gas,ch})^{\gamma}}\right)\right) \quad (58)$$

where $t_{w,max}$ is the maximum water thickness that accumulates in the GDL under the rib. This value was determined by neutron radiography experiments [28], which is approximately 50 μm.

The average liquid saturation in the GDL under the rib can be calculated from

$$s_{ca,gdl,rib} = \frac{t_{ca,gdl,rib}\, A_{seg}}{t_{gdl}\, A_{seg}\, \varepsilon} = \frac{t_{ca,gdl,rib}}{t_{gdl}\, \varepsilon} \quad (59)$$

where t_{gdl} is the GDL thickness, A is the segment area, and ε is the porosity of GDL.

The liquid saturation in the GDL under the channel is calculated from Refs. [11,36]:

$$N_{ca,w,gdl,ch} = -\frac{\rho_w K K_{rw}}{M_w \mu_w}\left(\frac{dP_{cap}}{ds}\right)\frac{ds}{dz} \quad (60)$$

At steady-state, $N_{ca,w,gdl,ch}$ is equal to the net water flux from anode to cathode and is determined by the membrane hydration model. Then saturation s can be obtained by solving Eq. (60).

In this model, we need to determine the amount of liquid water transport through the GDL under the channel $N_{ca,w,gdl,ch}$ and through the GDL under the rib $N_{ca,w,gdl,rib}$. We assume the water transport through the GDL under the channel is inversely proportional to the gas flow rate in the channel, which is similar to our analysis of water accumulation in the GDL under the channel in our former study; i.e. $C_{gc} = \alpha/N_{ca}$ [28].

$$N_{ca,w,gdl,ch} = \frac{\beta}{N_{ca,react,ch}} \quad (61)$$

Once we determine the water transport in the GDL under the channel, we can calculate the distribution of liquid saturation in the GDL by using Eq. (60). To simplify the problem, the capillary pressure gradient with respect to liquid saturation in Eq. (60) is assumed to be constant and equal to 22.95 N m^{-2} [35]. Then the liquid saturation in the catalyst layer can be obtained.

α, β, and γ in Eqs. (58) and (61) are calibrated based on experimental results. We calculate liquid saturations in the GDL under the channel and under the rib separately. The average value between these two variables is then used in the segment voltage model.

2.3. Membrane hydration model

The water transport within membranes is represented by the membrane hydration model shown in Fig. 2. There are three causes for water flux in the membrane: electro-osmotic drag from anode to cathode; back diffusion due to the concentration potential difference between the anode and cathode; and water generation at the cathode catalyst layer. These three factors are explained in the following.

The electro-osmotic drag is defined as

$$N_{w,osmotic} = K_{osmotic}\frac{I_{seg}}{F} \quad (62)$$

where $K_{osmotic}$ is the osmotic drag coefficient [3,37–40]. In this study, we use Springer's result [3]:

$$K_{osmotic} = \frac{2.5\lambda_{pem}}{22} \quad (63)$$

The water content in the membrane λ_{pem}, is calculated from the water activity of membrane a_{pem}:

$$\lambda_{pem} = 0.043 + 17.81 a_{pem} - 39.85 a_{pem}^2 + 36.0 a_{pem}^3, \quad 0 < a_{pem} \le 1 \quad (64)$$

The average water activity of anode and cathode is used to calculate the water content in the membrane:

$$a_{pem} = \frac{a_{an} + a_{ca}}{2} \quad (65)$$

In Eq. (65), a_{an} and a_{ca} are the RH of anode and cathode.

The water transport by back diffusion is expressed as

$$N_{w,diff} = K_{diff}\frac{c_{w,ca} - c_{w,an}}{t_{pem}} \quad (66)$$

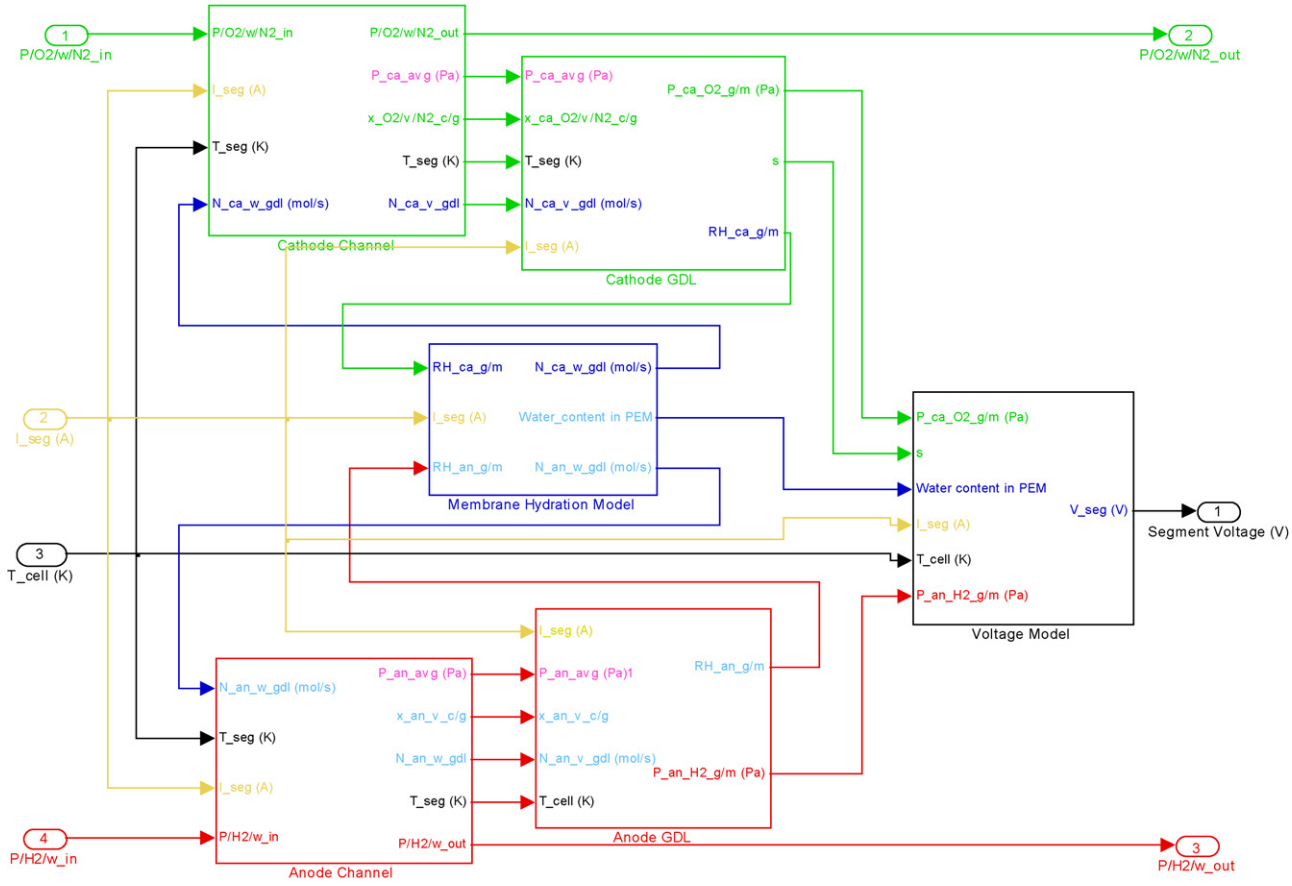

Fig. 4. Connection of six sub-models in the SIMULINK environment.

where c_w is the water concentration of the membrane as defined in Fuller's study [4], and t_{pem} is the membrane thickness. Water concentration is calculated as

$$c_{w,an} = \frac{\rho_{pem}}{M_{pem}}\lambda_{an} \tag{67}$$

$$c_{w,ca} = \frac{\rho_{pem}}{M_{pem}}\lambda_{ca} \tag{68}$$

where λ_{an} and λ_{ca} are calculated from the water activity in anode and cathode:

$$\lambda_{an} = 0.043 + 17.81a_{an} - 39.85a_{an}^2 + 36.0a_{an}^3, \quad 0 < a_{an} \le 1 \tag{69}$$

$$\lambda_{ca} = 0.043 + 17.81a_{ca} - 39.85a_{ca}^2 + 36.0a_{ca}^3, \quad 0 < a_{ca} \le 1 \tag{70}$$

In Eq. (66), K_{diff} is the back diffusion coefficient and is a function of temperature and water content in the membrane [3,41]:

$$K_{diff} = K_\lambda \exp\left(2416\left(\frac{1}{303} - \frac{1}{T_{seg}}\right)\right) \tag{71}$$

where[1]

$$K_\lambda = \begin{cases} 10^{-10} & ,\lambda_{pem} < 2 \\ 10^{-10}(1 + 2(\lambda_{pem} - 2)) & ,2 \le \lambda_{pem} \le 3 \\ 10^{-10}(3 - 1.167(\lambda_{pem} - 3)) & ,3 < \lambda_{pem} \le 4.5 \\ 1.25 \times 10^{-10} & ,\lambda_{pem} \ge 4.5 \end{cases} \tag{72}$$

[1] The value 1.167 is used instead of 1.67. If 1.67 is used in this equation, there will be a "discontinuity" when calculating K_λ at λ_{pem}=4.5 by using the 3rd and the 4th equations.

The net water flux through the anode GDL is

$$N_{an,w,gdl} = N_{w,diff} - N_{w,osmotic} \tag{73}$$

whereas that through the cathode GDL is

$$N_{ca,w,gdl} = N_{w,osmotic} - N_{w,diff} + \frac{I_{seg}}{2F} \tag{74}$$

where the last term of Eq. (74) is the water generation at the cathode catalyst layer. The water content is used to calculate the membrane conductivity in the segment voltage model, and water fluxes in anode and cathode are used in the GDL models and the flow channel models.

2.4. Segment voltage model

The segment voltage model calculates voltage of each segment at specific current according to the partial pressures of hydrogen and oxygen, membrane water content, and temperature. The segment voltage can be expressed as

$$V_{seg} = V_{rev} - V_{act} - V_{ohm} - V_{conc} \tag{75}$$

where V_{rev}, V_{act}, V_{ohm} and V_{conc} are the theoretical reversible voltage, the activation overpotential, the ohmic overpotential, and the concentration overpotential, respectively.

The theoretical reversible voltage is calculated from Ref. [42]:

$$\begin{aligned} V_{\text{rev}} &= \frac{-\Delta G}{2F} \\ &= \frac{-\Delta G^0}{2F} + \frac{RT_{\text{seg}}}{2F} \ln\left(\frac{P_{\text{H}_2} P_{\text{O}_2}^{0.5}}{P_{\text{H}_2\text{O}}}\right) \\ &= 1.229 - 0.85 \times 10^{-3}(T_{\text{seg}} - 298.15) \\ &\quad + 4.3085 \times 10^{-5} T_{\text{seg}} \left[\ln(P_{\text{an,H}_2,\text{g/m}}) + \frac{1}{2}\ln(P_{\text{ca,O}_2,\text{g/m}})\right] \end{aligned} \tag{76}$$

The partial pressures of hydrogen $P_{\text{an,H}_2,\text{g/m}}$ and oxygen $P_{\text{ca,O}_2,\text{g/m}}$ come from the anode/cathode GDL models.

The activation overpotential arises from the kinetic reaction at the anode and cathode. Due to slower kinetics of oxygen reduction at the cathode side, the voltage drop due to activation overpotential is dominated by the cathode. The overpotential is modified from the study in Ref. [25] as

$$V_{\text{act}} = 0.2 + 0.1[1 - \exp(-20 i_{\text{seg}})] \tag{77}$$

where i_{seg} is the current density of a segment.

The ohmic overpotential is due to the internal resistance of a segment and is expressed as

$$V_{\text{ohm}} = I_{\text{seg}} R_{\text{seg}} \tag{78}$$

where I_{seg} is the segment current. The resistance of the segment is the sum of all components through which current flows and contact resistance. These components are membrane, GDLs, and flow field plates:

$$R_{\text{seg}} = R_{\text{pem}} + R_{\text{gdl}} + R_{\text{plate}} + R_{\text{contact}} \tag{79}$$

The conductivities of GDL and graphite plates are typically much larger than that of the membrane, so it is not necessary to consider their resistances. Thus only the membrane resistance and contact resistance are considered in this model. The membrane resistance is obtained from

$$R_{\text{pem}} = \frac{t_{\text{pem}}}{\sigma_{\text{pem}} A_{\text{seg}}} \tag{80}$$

where the membrane conductivity σ_{pem} is a function of temperature and water content in the membrane, and is expressed in the form [3]:

$$\sigma_{\text{pem}} = (b_{11}\lambda_{\text{pem}} - b_{12})\exp\left[b_{13}\left(\frac{1}{303} - \frac{1}{T_{\text{seg}}}\right)\right] \tag{81}$$

where b_{11}, b_{12}, and b_{13} are empirically determined from our experimental results.

Concentration overpotential results from the change in concentration of the reactants as they are consumed in the reaction. The concentration overpotential derived from the Nernst equation is modified from Ref. [43]. In addition, the flooding effect should also be considered, which reduces the activation area of the catalyst, so the maximum current density is reduced when liquid water appears in the catalyst layer. The modified concentration overpotential is expressed as

$$V_{\text{conc}} = b_{21} i_{\text{seg}}^{b_{22}} \ln\left(1 - \frac{i_{\text{seg}}}{i_{\text{limit}}(1-s)}\right) \tag{82}$$

where b_{21} and b_{22} are coefficients to be determined by experimental data.

In the above calculations, the current density in each segment is assumed to be known and the same. However, the cell voltage of all segments should be the same, and the difference in humidity, reactant pressure, etc. resulted in different current density. After each segment voltage model calculates its voltage, actual segment current can be corrected by enforcing all the segment voltages to be the same.

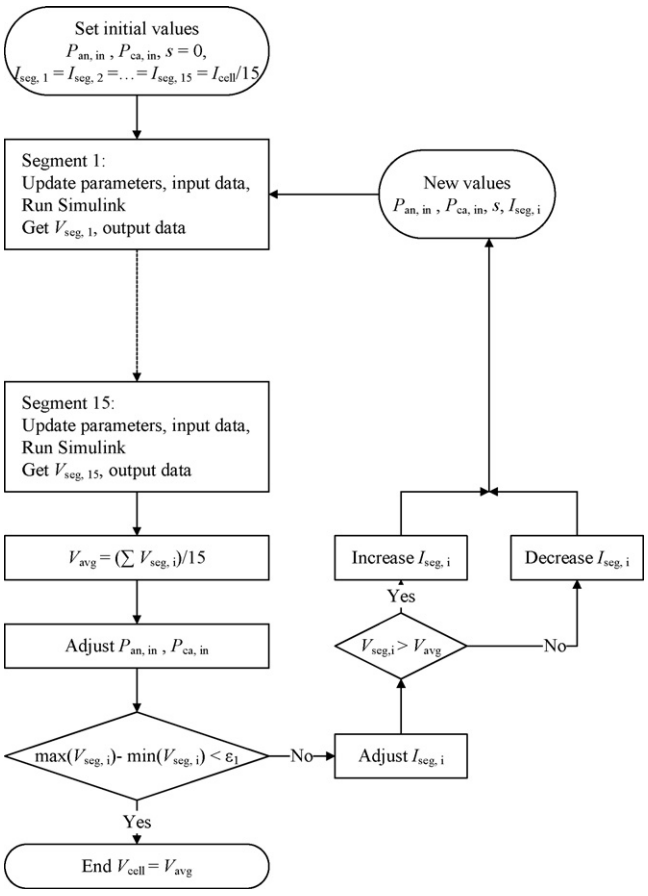

Fig. 5. Flow diagram of solving cell voltage.

2.5. Cell voltage calculation

The models presented in the previous sub-sections are implemented in the SIMULINK environment. The block diagrams of six sub-models of a segment are shown in Fig. 4. Given the inflow properties and (initial guess of) segment current, the segment model calculates the segment voltage. Since the current density is actually not uniform throughout the active area of the cell. The cell voltage is determined iteratively by the process shown in Fig. 5. At the beginning, we guess an inlet gas pressure P_{in} and a cell current I_{cell}. The initial guess for segment currents $I_{\text{seg},i}$, is set to be one 15th

Table 1
Specification of the single cell used in this study

Parameter	Value
Cell active area (A_{cell})	100 cm^2
Channel depth (H_{ch})	1 mm
Channel width (W_{ch})	1.6 mm
Rib width (W_{rib})	1.7 mm
Anode channel number in a segment (Z_{an})	6
Cathode channel number in a segment (Z_{ca})	10
Anode channel length in a segment (L_{an})	3.33 cm
Cathode channel length in a segment (L_{ca})	2 cm
GDL thickness (t_{gdl})	184 μm
GDL porosity (ε)	0.725
Dry membrane thickness (t_{pem})	25 μm
Dry membrane density (ρ_{pem})	2000 kg m^{-3}
Dry membrane equivalent weight (M_{pem})	1.1 kg mol^{-1}

Table 2
Parameter values that obtained from literature

Parameter	Value
Absolute permeability of GDL (K)	1×10^{-8} m^{-2} [11]
Relative permeability of GDL (K_{rw})	S [12]
Dynamic viscosity of hydrogen (μ_{H_2})	9.5493×10^{-6} N s m^{-2} [29]
Dynamic viscosity of oxygen (μ_{O_2})	2.2379×10^{-5} N s m^{-2} [29]
Dynamic viscosity of nitrogen (μ_{N_2})	1.9260×10^{-5} N s m^{-2} [29]
Dynamic viscosity of water vapor (μ_v)	4.6657×10^{-4} N s m^{-2} [29]
Pressure-diffusivity product of water vapor and hydrogen pair (PD_{H_2-v})	16.6801 Pa m^2 s^{-1} [30]
Pressure-diffusivity product of water vapor and oxygen pair (PD_{O_2-v})	3.2890 Pa m^2 s^{-1} [30]
Pressure-diffusivity product of water vapor and nitrogen pair (PD_{v-N_2})	3.4400 Pa m^2 s^{-1} [30]
Pressure-diffusivity product of oxygen and nitrogen pair ($PD_{O_2-N_2}$)	2.5504 Pa m^2 s^{-1} [30]
Diffusivity of water vapor in hydrogen (D_{v-H_2})	9.3940×10^{-3} m^2 s^{-1} [30]
Diffusivity of water vapor in air ($D_{v\text{-air}}$)	2.6560×10^{-3} m^2 s^{-1} [30]

of the cell current, I_{cell}. The segment voltage $V_{seg,i}$ is determined by the segment model described in the previous section.

If the difference between the maximum and minimum segment voltages is not within an acceptable range, the segment currents need to be corrected. Based on the typical polarization curve of a fuel cell, the segment with higher voltage should increase its current, and that with lower voltage should decrease its current. To increase the iteration speed, the increase in segment current is set to be proportional to the voltage difference while keeping the cell current constant. In addition, the inlet pressures of the anode and cathode are also adjusted to keep the outlet pressure the same as the ambient pressure.

2.6. Tuning parameters

We designed a single cell and conducted neutron radiography experiments to adjust water related parameters in this model. The fuel cell specification and corresponding parameters are listed in Table 1. Those parameter values obtained from the literature are listed in Table 2. The parameters that are adjusted in this paper are listed in Table 3.

In the ohmic overpotential region, membrane conductivity is mainly affected by water content in the membrane, as shown in Eq. (81). Thus, b_{11}, b_{12}, and b_{13} in Eq. (81) and the contact resistance $R_{contact}$ in Eq. (79) were tuned to match the calculated I–V curve to with experimental data in the ohmic overpotential region. α and γ in Eq. (58) and β in Eq. (61) were adjusted based on water thickness obtained by neutron radiography experiments. Once α, β, and γ were determined, liquid saturation can be determined. Subsequently, b_{21}, b_{22}, and i_{limit} in Eq. (82) are adjusted according to the concentration overpotential region of I–V curve.

Table 3
Parameters that tuned based on experimental data

Parameter	Eq. number	Tuned value
$R_{contact}$	(79)	0.047
α	(58)	−0.012
β	(61)	1×10^{-9}
γ	(58)	2
b_{11}	(81)	0.195
b_{12}	(81)	0.326
b_{13}	(81)	350
b_{21}	(82)	−0.75
b_{22}	(82)	7
i_{limit}	(82)	1.2

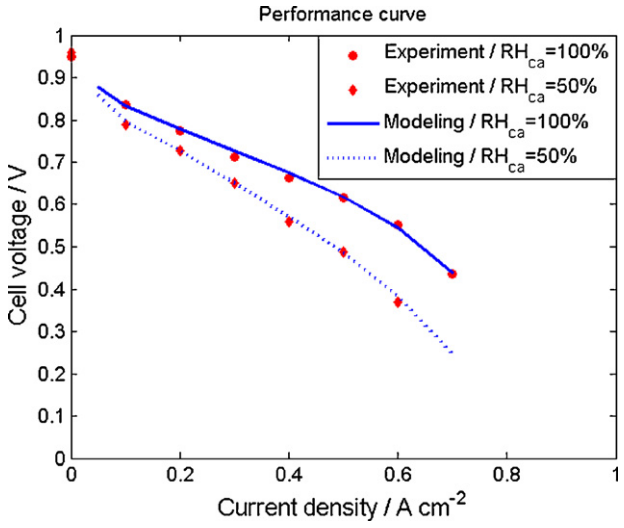

Fig. 6. Comparison of experimental results and modeling results for different cathode inlet RH.

3. Results and discussions

In practical applications, due to space and cost considerations, it is common to humidify only the cathode reactant. Thus, we will focus on the influence of RH of cathode inlet on cell performance and water transport. Fig. 6 compares the cell performance curves obtained by this model and by experiments. The cell operating at low cathode inlet RH of 50% shows lower cell performance. This is because the under-saturated air takes water from the membrane, resulting in low membrane hydration and conductivity.

In this study, each segment is regarded as a lumped model. Thus, at the end of iteration procedure, only average values will be obtained. For visual aids, colorful pictures are created through interpolation and extrapolation of these values, which are marked at the center of each segment.

3.1. Distribution of current density and water content in the membrane

Membrane dehydration increases ohmic overpotential, and could even cause irreversible damage to the membrane. Since the membrane conductivity dominates (conductivity of membrane: ~2.75 Ω^{-1} m^{-1}; GDL: ~1250 Ω^{-1} m^{-1}; graphite plate:

Table 4
List of selected operating conditions

	Case 1	Case 2	Case 3	Case 4
Anode/cathode inlet RH (%)	0/100	0/50	0/100	0/50
Anode/cathode stoichiometry value	1.2/3	1.2/3	1.2/3	1.2/3
Anode/cathode outlet pressure (atm)	1/1	1/1	1/1	1/1
Cell current density (A cm^{-2})	0.7	0.6	0.1	0.1
Cell temperature (°C)	70	70	70	70

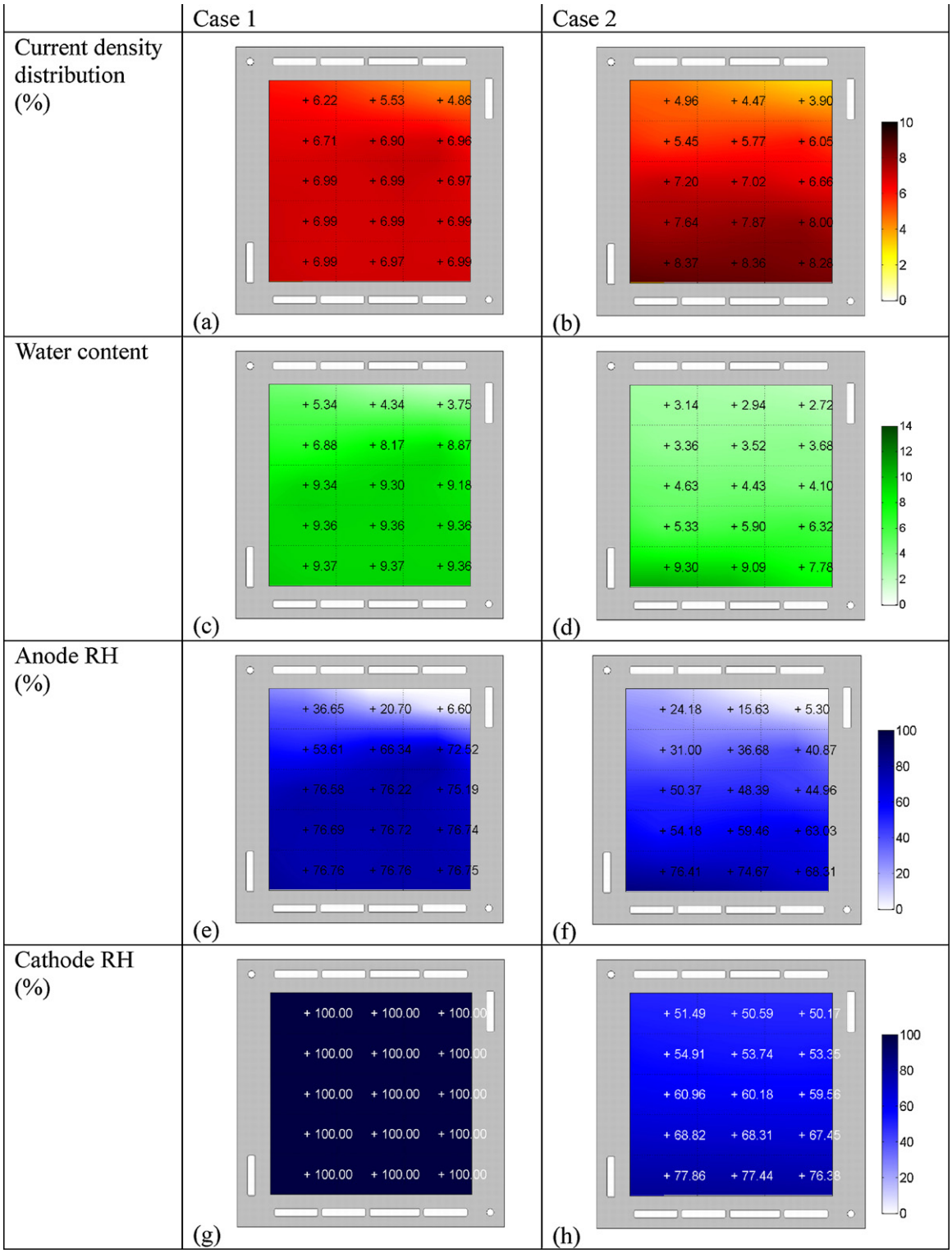

Fig. 7. Distribution of (a) and (b) current density; (c) and (d) water content in the membrane; (e) and (f) RH in the anode channel; (g) and (h) RH in the cathode channel. Left figures: case 1. Right figures: case 2.

$\sim 1 \times 10^5\ \Omega^{-1}\ m^{-1}$), current density distribution is highly dependent on the water content in the membrane, which in terms significantly influences the cell performance and reliability.

Figs. 7(a) and (b) and 8(a) and (b) show current density distribution of four selected operating conditions, as listed in Table 4. All figures suggest that maximum current are located near the anode outlet, the region with maximum water content. By comparing Fig. 7(a) and (b) (high current density cases), we observe that at fully humidified cathode condition, the maximum local current is approximately 1.4 times the minimum local current. However, this ratio increases to 2 at low cathode humidity condition. In Fig. 8(a) and (b), for low current density cases, the maximum local current

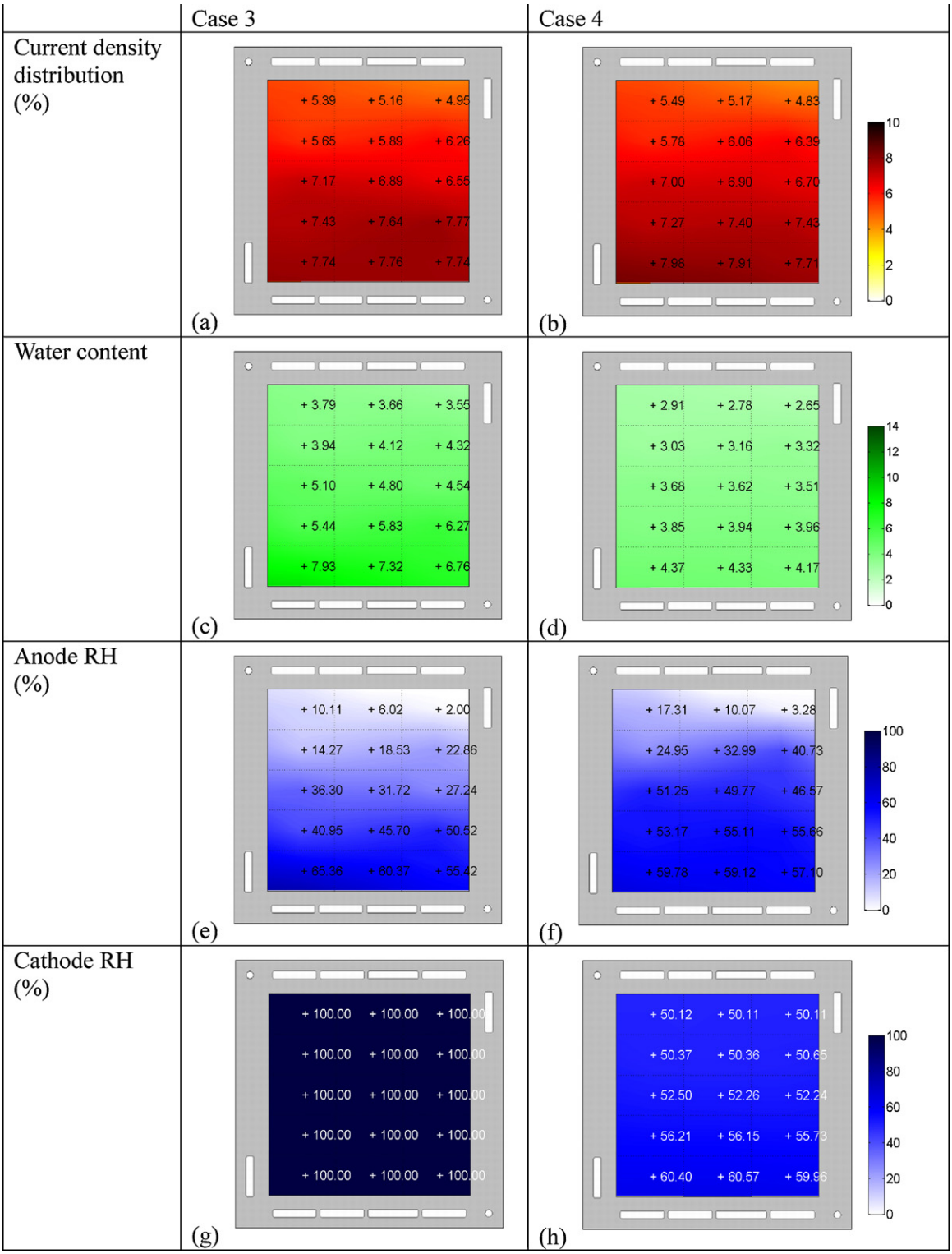

Fig. 8. Distribution of (a) and (b) current density; (c) and (d) water content in the membrane; (e) and (f) RH in the anode channel; (g) and (h) RH in the cathode channel. Left figures: case 3. Right figures: case 4.

is 1.5 and 1.6 times of the minimum, respectively. The result suggests that at low current density, cathode inlet RH has less influence on current density distribution. Low cathode humidity causes low water content, as shown in Fig. 8(d).

A few methods to measure current density distribution were developed in the literature [44–47]. For example, divided current collectors can be used to measure local current flow. Yoshioka et al. [44] compared the distribution of current densities at different inlet gas RH levels. Their results show that the region close to air inlet has lower current density. The trend is more significant with dry inlet air. Liu et al. [45] measured current density distribution of a fuel cell with one serpentine flow channel. Their findings are

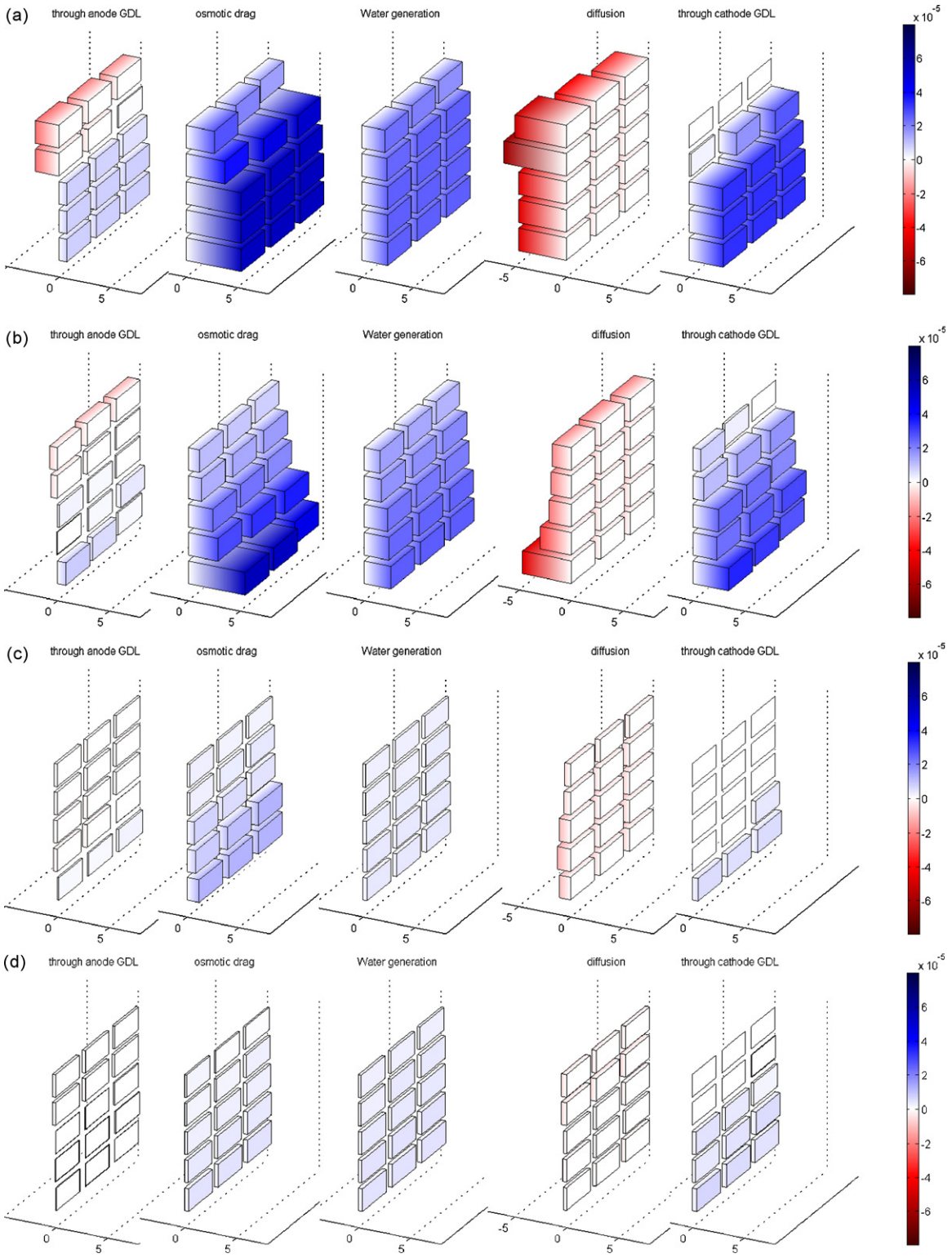

Fig. 9. Quantity of water transport (mol s^{-1}) across the MEA. (a) Case 1; (b) case 2; (c) case 3; (d) case 4.

the same as [44] qualitatively, except that with fully humidified air, current density of the area near outlet is lower due to flooding. In our study, the effect of flooding on reducing current density near outlet is not obvious. A possible reason is that anode reactant is not humidified so the excess water transports to the anode. Another reason is that we use straight parallel cathode channels so liquid water is quickly removed from channels.

3.2. Distribution of RH in the flow channel and water transport in the MEA

Figs. 7(e) and (f) and 8(e) and (f) show the RH distribution in the anode flow channel. For all cases, RH increases along the flow direction because dry hydrogen gradually uptakes water vapor that comes from the cathode by back diffusion. Fig. 9 compares water

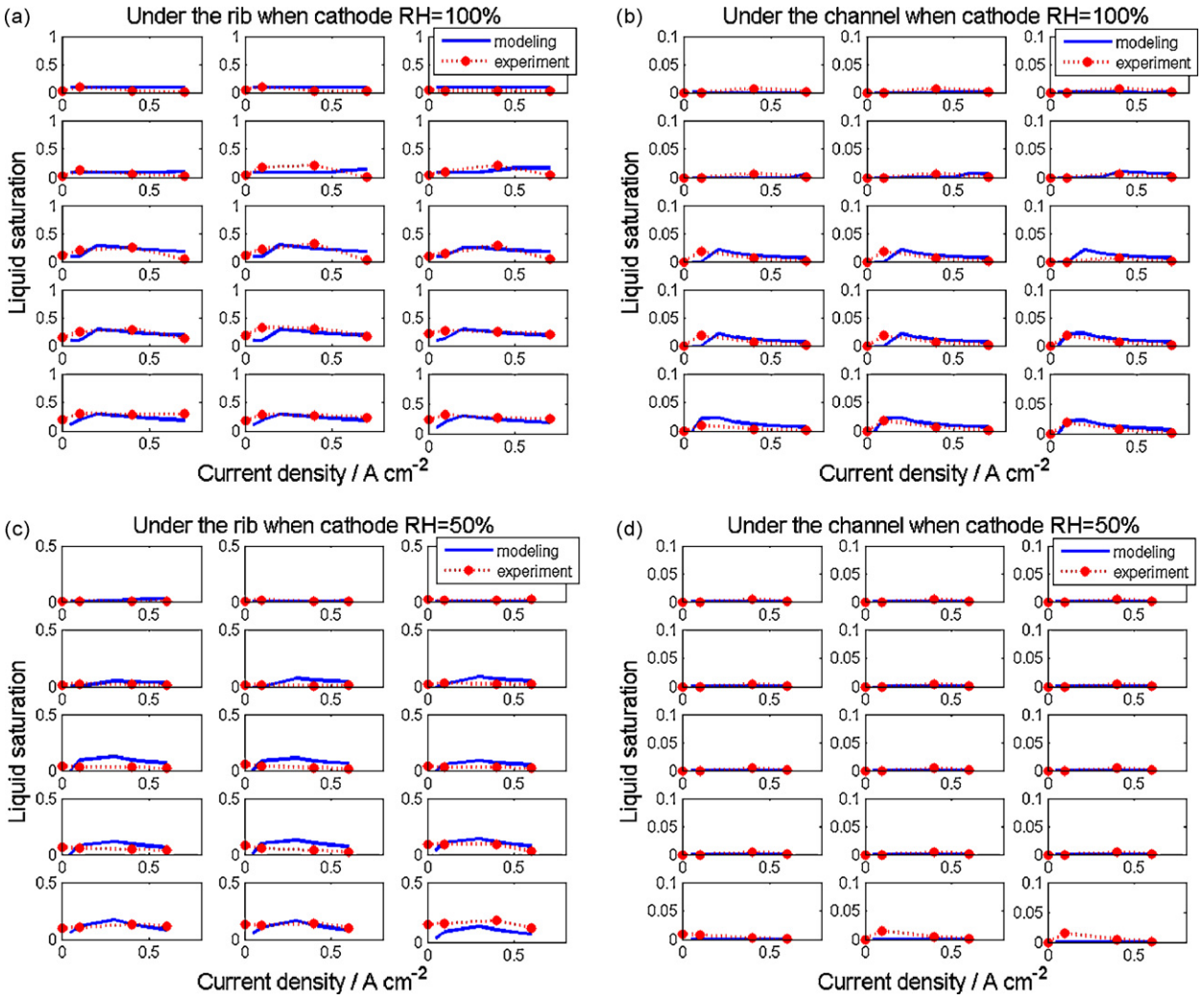

Fig. 10. Comparison of modeling results and experimental data. (a) Distribution of liquid saturation in the GDL under the rib when cathode inlet RH = 100%; (b) distribution of liquid saturation in the GDL under the channel when cathode inlet RH = 100%; (c) distribution of liquid saturation in the GDL under the rib when cathode inlet RH = 50%; (d) distribution of liquid saturation in the GDL under the channel when cathode inlet RH = 50%.

transport through the membrane and through both anode and cathode GDLs. The magnitude indicates the quantity of water transport and positive represents the direction from the anode to the cathode. At high current density, water transport from the anode channel to the membrane through the anode GDL was observed in the downstream segments, as shown in Fig. 9(a) and (b). The high current density in those segments results in high electro-osmotic drag from the anode to the cathode, which is stronger than the back diffusion from the cathode to the anode; hence, water in the anode reactant supplies for the difference. However, as shown in Fig. 7(a), the anode RH does not decrease along flow channel. Because of hydrogen consumption along flow channel, the molar fraction of water vapor increases along flow channel. That also explains why RH in the anode downstream segments barely increased.

Fig. 9(c) and (d) shows that the electro-osmotic drag of the segments near outlet in case 3 is significantly higher than that in case 4, although current densities of both cases are quite similar, as shown in Fig. 8(a) and (b). According to Eq. (63), the electro-osmotic drag coefficient is a function of water content. Thus, high water content in the membrane is attributed to humidified cathode reactant.

Figs. 7(g) and 8(g) show fully saturated reactant in the cathode channel throughout the active area. Since cathode inlet reactant is fully humidified, the generated water transports to the channel in liquid form. In the cases of under-saturated cathode inlet reactant, the cathode RH gradually increases along the gas flow direction, as shown in Figs. 7(h) and 8(h). The increase is due to water generation and also oxygen consumption along the flow channel, resulting in increased molar fraction of water vapor. Water transports through GDLs influences diffusivities of reactant and may also form liquid water in the GDL, which increases concentration overpotential.

3.3. Distribution of water accumulation

Cathode liquid saturation in the GDL affects cell performance because liquid water may cover the reaction sites in the catalyst layer or block the pathway of gas flow through the GDL. The liquid saturation in the cathode GDL is affected by many factors: cell temperature, permeability and hydrophobicity of GDL, net water flux through the GDL, and cathode flow RH. In this model, temperature, permeability and hydrophobicity of GDL are assumed to be constant. Under-saturated condition, net water flux through GDL is determined by operating current density. Higher current density results in higher electro-osmotic drag and water generation, which causes higher net water flux through GDL, as shown in Fig. 9(a) and (b).

Fig. 10 compares average liquid saturation in the cathode GDL of modeling results and experimental data. The 15 subplots correspond to 15 segments of the active area. Fig. 10(a) and (c) suggests that liquid water accumulate in the GDL under the rib. Results from other neutron radiography experiments also show this phenomenon [48,49]. Slight liquid saturation in the GDL under the rib is observed at the segment near cathode inlet and increases toward the outlet. Maximum liquid saturation is approximately 0.4. The low water accumulation in the cathode GDL at high current density is likely due to the high gas flow rate at high current density. Fig. 10(c) shows some liquid saturation in the GDL under the rib when cathode inlet RH is 50%. However, there is almost no liquid water in the GDL under the channel, as shown in Fig. 10(d). This is because the gas flow in the flow channel is under-saturated.

4. Conclusions

In this study a segmented fuel cell model was developed. Each segment is viewed as a lumped model, which consists of six interacting sub-models, and is connected based on the reactant flow directions. This model is calibrated based on experimental results and is able to describe liquid water saturation in the GDL under the channel and in the GDL under the rib. The calibrated model was used to investigate distributions of current density, water content in the membrane, RH in the anode/cathode, and water accumulation in the GDL under the channel/rib as well as water transport in the MEA.

Modeling results show that cathode inlet RH has significant influence on the uniformity of water content in the membrane and current density. At low cathode inlet humidity and high load, the maximum local current density is twice that of the minimum local current density. Cathode humidity has less influence on the uniformity of current density at low current load. In this study, the influence of water accumulation on current density is not obvious. That could be due to un-humidified hydrogen, short flow channels, and operating current density.

Water transport mechanisms across the MEA were demonstrated in this study. The amount of water transport in different location was predicted by this segmented model. The results show current density and the amount of water transport influence with each other. This result also provides useful information in placing the inlet/oulet of anode/cathode when we design flow field patterns.

A model describing water accumulation in the GDL was proposed in this study. Liquid water tends to accumulate in the GDL under the rib due to the suppression of gas flow in the channel. Maximum liquid saturation in the GDL under the rib is observed near the outlet and the value is approximately 0.4 in this flow field design.

This study investigated the water content in the membrane and liquid water accumulation in the GDL for a specific designed single cell. For the future study, the concept of modeling will be applied on different flow field designs to study the influence of flow field design on water distribution in a fuel cell.

Acknowledgements

The authors would like to acknowledge the support from National Science Foundation (NSF0408664) for this study. The authors also would like to express their gratitude to the NIST Center for Neutron Research where neutron radiography and fuel cell test station were supported for experiments.

References

[1] D.M. Bernardi, M.W. Verbrugge, AIChE J. 37 (1991) 1151–1163.
[2] D.M. Bernardi, M.W. Verbrugge, J. Electrochem. Soc. 139 (1992) 2477–2491.
[3] T.E. Springer, T.A. Zawodzinski, S. Gottesfeld, J. Electrochem. Soc. 138 (1991) 2334–2342.
[4] T.F. Fuller, J. Newman, J. Electrochem. Soc. 140 (1993) 1218–1225.
[5] V. Gurau, H. Liu, S. Kakac, AIChE J. 44 (1998) 2410–2422.
[6] S. Um, C.Y. Wang, K.S. Chen, J. Electrochem. Soc. 147 (2000) 4485–4493.
[7] C.Y. Wang, W.B. Gu, B.Y. Liaw, J. Electrochem. Soc. 145 (1998) 3407–3417.
[8] S. Um, C.Y. Wang, K.S. Chen, J. Power Sources 125 (2004) 40–51.
[9] J.J. Baschuk, X. Li, J. Power Sources 86 (2000) 181–196.
[10] Z.H. Wang, C.Y. Wang, K.S. Chen, J. Power Sources 94 (2001) 40–50.
[11] U. Pasaogullari, C.Y. Wang, J. Electrochem. Soc. 151 (2004) A399–A406.
[12] D. Natarajan, T.V. Nguyen, J. Electrochem. Soc. 148 (2001) A1324–A1335.
[13] D. Natarajan, T.V. Nguyen, J. Power Sources 115 (2003) 66–80.
[14] G. Lin, T.V. Nguyen, J. Electrochem. Soc. 153 (2006) A372–A382.
[15] A. Turhan, K. Heller, J.S. Brenizer, M.M. Mench, J. Power Sources 160 (2006) 1195–1203.
[16] J. Zhang, D. Kramer, R. Shimoi, Y. Ono, E. Lehmann, A. Wokaun, K. Shinohara, G.G. Scherer, Electrochim. Acta 51 (2006) 2715–2727.
[17] Y.-S. Chen, H. Peng, D.S. Hussey, D.L. Jacobson, D.T. Tran, T. Abdel-Baset, M. Biernacki, J. Power Sources 170 (2007) 376–386.
[18] S. Maharudrayya, S. Jayanti, A.P. Deshpande, J. Power Sources 157 (2006) 358–367.
[19] S. Shimpalee, S. Greenway, J.W. Van Zee, J. Power Sources 160 (2006) 398–406.
[20] X. Liu, H. Guo, F. Ye, C.F. Ma, Electrochim. Acta 52 (2007) 3607–3614.
[21] US Patent: 5,981,098 (1999).
[22] US Patent: 6,893,708B2 (2005).
[23] W. Ying, T.-H. Yang, W.-Y. Lee, J. Ke, C.-S. Kim, J. Power Sources 145 (2005) 572–581.
[24] J.C. Amphlett, R.F. Mann, B.A. Peppley, P.R. Roberge, A. Rodrigues, J. Power Sources 61 (1996) 183–188.
[25] J.T. Pukrushpan, A.G. Stefanopoulou, H. Peng, IEEE Control Syst. Magazine 24 (2004) 30–46.
[26] Y. Shan, S.Y. Choe, J. Power Sources 145 (2005) 30–39.
[27] M. Wang, H. Guo, C. Ma, J. Power Sources 157 (2006) 181–187.
[28] Y.-S. Chen, H. Peng, ASME, The Fifth International Conference on Fuel Cell Science, Engineering and Technology, 2007.
[29] R.W. Fox, A.T. McDonald, Introduction to Fluid Mechanics, John Wiley & Sons, Inc., New York, USA, 1994.
[30] J. Benitez, Principles and Modern Applications of Mass Transfer Operations, John Wiley & Sons, Inc., New York, USA, 2002.
[31] T.E. Springer, M.S. Wilson, S. Gottesfeld, J. Electrochem. Soc. 140 (1993) 3513–3526.
[32] Rohsenow, Handbook of Heat Transfer, 3rd, McGraw-Hill, New York, 1998.
[33] J.S. Yi, T.V. Nguyen, J. Electrochem. Soc. 146 (1999) 38–45.
[34] W.H. He, J.S. Yi, T.V. Nguyen, AIChE J. 46 (2000) 2053–2064.
[35] G. Lin, W. He, T.V. Nguyen, J. Electrochem. Soc. 151 (2004) A1999–A2006.
[36] J.H. Nam, M. Kavinay, Int. J. Heat Mass Transfer 46 (2003) 4595–4661.
[37] T.F. Fuller, J. Newman, J. Electrochem. Soc. 139 (1992) 1332–1339.
[38] Th.A. Zawodzinski, S. Radzinski, R.J. Sherman, V.T. Smith, T.E. Springer, S. Gottesfeld, J. Electrochem. Soc. 140 (1993) 1041–1047.
[39] G. Xie, T. Okada, J. Electrochem. Soc. 142 (1995) 3057–3062.
[40] T.A. Zawodzinski, J. Davey, J. Valerio, S. Gottesfeld, Electrochim. Acta 40 (1995) 297–302.
[41] S. Dutta, S. Shimpalee, J.W. Van Zee, Int. J. Heat Mass Transfer 44 (2001) 2029–2042.
[42] J. Larminie, A. Dicks, Fuel Cell Systems Explained, Wiley, 2003.
[43] G. Squadrito, G. Maggio, E. Passalacqua, F. Lufrano, A. Patti, J. Appl. Electrochem. 29 (1999) 1449–1455.
[44] S. Yoshioka, A. Yoshimura, H. Fukumoto, O. Hiroi, H. Yoshiyasu, J. Power Sources 144 (2005) 146–151.
[45] Z. Liu, Z. Mao, B. Wu, L. Wang, V.M. Schmidt, J. Power Sources 141 (2005) 205–210.
[46] P.C. Ghosh, T. Wüster, H. Dohle, N. Kimiaie, J. Mergel, D. Stolten, J. Power Sources 154 (2006) 184–191.
[47] N. Rajalakshmi, M. Raja, K.S. Dhathathreyan, J. Power Sources 112 (2002) 331–336.
[48] R. Mukundan, J.R. Davey, T. Rockward, J.S. Spendelow, B.S. Pivovar, D.S. Hussey, D.L. Jacobson, M. Arif, R.L. Borup, ECS Trans. 11 (2007) 411–422.
[49] A. Turhan, K. Heller, J.S. Brenizer, M.M. Mench, J. Power Sources 180 (2008) 773–783.